Commun. Comput. Phys.
doi: 10.4208/cicp.120515.280815a

Vol. **19**, No. 1, pp. 251-272
January 2016

Effect of Oscillation Structures on Inertial-Range Intermittence and Topology in Turbulent Field

Kun Yang[1], Zhenhua Xia[1], Yipeng Shi[1,*] and Shiyi Chen[1,2]

[1] *State Key Laboratory of Turbulence and Complex Systems, Center for Applied Physics and Technology, College of Engineering, Peking University, Beijing 100871, P.R. China.*
[2] *Collaborative Innovation Center of Advanced Aero-Engine, Beijing 100191, P.R. China.*

Received 12 May 2015; Accepted (in revised version) 28 August 2015

Abstract. Using the incompressible isotropic turbulent fields obtained from direct numerical simulation and large-eddy simulation, we studied the statistics of oscillation structures based on local zero-crossings and their relation with inertial-range intermittency for transverse velocity and passive scalar. Our results show that for both the velocity and passive scalar, the local oscillation structures are statistically scale-invariant at high Reynolds number, and the inertial-range intermittency of the overall flow region is determined by the most intermittent structures characterized by one local zero-crossing. Local flow patterns conditioned on the oscillation structures are characterized by the joint probability density function of the invariants of the filtered velocity gradient tensor at inertial range. We demonstrate that the most intermittent regions for longitudinal velocity tend to lay at the saddle area, while those for the transverse velocity tend to locate at the vortex-dominated area. The connection between the ramp-cliff structures in passive scalar field and the corresponding saddle regions in the velocity field is also verified by the approach of oscillation structure classification.

PACS: 47.27.eb, 47.27.Gs
Key words: Oscillation structure, intermittency, transverse velocity, passive scalar.

1 Introduction

Inertial-range intermittency is a well-known feature in turbulent flows quantified by the anomalous scaling of structure functions $S_p(r)$. In isotropic velocity field, $S_p(r)$ can be either the longitudinal structure function $S_p(r)=\langle|\delta_r u|^p\rangle$, or the transverse structure function $S_p^T(r)=\langle|\delta_r v|^p\rangle$. Here $\langle\cdots\rangle$ denotes the ensemble average, $\delta_r u=u(x+r/2)-u(x-r/2)$

*Corresponding author. *Email addresses:* yangkun86@foxmail.com (K. Yang), xiazh1006@gmail.com (Z. Xia), ypshi@coe.pku.edu.cn (Y. Shi), syc@coe.pku.edu.cn (S. Chen)

and $\delta_r v = v(x+r/2) - v(x-r/2)$, where u and v are the velocity components in the same and normal directions to the separation r, respectively. Kolmogorov's similarity theory [1,2] predicted the simple scaling behavior that $S_p(r) \sim r^{\zeta_p}$ and $S_p^T(r) \sim r^{\zeta_p^T}$, with both ζ_p and ζ_p^T equal to $p/3$. Experimental measurements and numerical simulations showed that the scaling exponents ζ_p and ζ_p^T depart from $p/3$ when $p \neq 3$ [3–10]. The intermittent behavior has also been observed in the passive scalar field θ [5, 11, 12], that the structure function $S_p^\theta(r)$ has a scaling ξ_p departing from $p/3$ as predicted by the KOC theory of Obukhov [13] and Corrsin [14], where $S_p^\theta(r) = \langle |\delta_r \theta|^p \rangle$ and $\delta_r \theta = \theta(x+r/2) - \theta(x-r/2)$.

Many models have been proposed to describe the anomalous scaling of structure functions of velocity [3, 15–19] and passive scalar [20–24]. These models present more and more accurate depiction of the scaling exponents, however the essence of intermittence remains to be an open issue, and the corresponding debates are briefly summarized as follows:

(1) For the longitudinal velocity structure function, it was predicted that the intense vortex structures are responsible for the inertial-range intermittency [18, 25, 26], while Sain et al. [27] argued that the existence of vortex filaments is not crucial for the anomalous scaling.

(2) For the transverse velocity structure function, plenty of works have been devoted to clarify whether ζ_p^T should be equal to ζ_p. Biferale and Procaccia [28] stated that ζ_p^T should be equal to ζ_p theoretically, and this relation appears to be supported by some experimental measurements [29, 30]. On the other hand, many experimental results [6,31,32] and numerical simulations [4,33] suggest that these two scalings are different. It is argued that anisotropy [34,35] and finite Reynolds number effects [34,36] have large contribution to the difference between the ζ_p^T and ζ_p, while the discrepancy can still be observed in the experimental measurement at Reynolds number of about 10^4 [6] and DNS fields where the isotropy can be welly maintained [7–10]. Boratav and Pelz [33] inferred that the difference of ζ_p^T and ζ_p is due to an imbalance contribution to intermittency of the enstrophy-dominated and the strain-dominated regions. Chen et al. [19] studied the relation between enstrophy and $S_p^T(r)$, and proposed the refined similarity hypothesis for transverse velocity increments, which is verified by their DNS data and further supported by the experimental measurement of Zhou et al. [37].

(3) For the passive scalar field, it was shown that when a mean gradient of passive scalar was imposed, the ramp-cliff structures would cause the isotropy to be violated at very small scales [11,12,38,39]. Warhaft conjectured that the departure from local isotropy at the small scales and the internal intermittency are intimately related [11]. However, to the best of our knowledge, no work has provided a clear description about the connection between the flow structures and the inertial-range intermittency of passive scalar.

In the companion paper [40], the effect of the geometric properties on the anomalous scaling of longitudinal velocity structure function was studied, using the newly developed oscillation structure (OS) classification based on local zero-crossings. It was found

that the oscillation structure with only one local zero-crossing is the main contribution for inertial-range intermittency. In the present work, the same procedure is applied to the transverse velocity and passive scalar to study the relation of oscillation structures and inertial-range intermittency for these two fields. To further explore the flow structure property in the most intermittent regions of longitudinal velocity, transverse velocity and passive scalar, the OS classification is combined with the topological approach developed by Chong et al. [41]. This topological approach is based on the relations of three invariants of the deformation rate tensor of the velocity field, and it can discern the vortex and saddle patterns in the flow field. The combination of these two methods is a more intuitive approach compared with the statistical analysis in previous studies.

In this paper, a forced isotropic turbulence obtained by direct numerical simulation (DNS) is used to study the relation between OS subclasses, inertial-range intermittency and topological structures in both the velocity and passive scalar field. The relation between the OS subclasses and intermittency is also verified in a flow field obtained by large-eddy simulation (LES) to examine the Reynodes number effect on the results. Meanwhile, a self-similar field, i.e. the fractal Brownian motion (FBM) [42] is also studied by the same approach as a comparison.

The outline of this paper is as follows. In Section 2, the numerical methods on the generation of the turbulent fields and the fractal Brownian motion, and the procedure of oscillation structure classification are briefly described. The detailed results are presented and discussed in Section 3. Some concluding remarks are finally addressed in Section 4.

2 Numerical methods

2.1 DNS and LES

The governing equations for the DNS of velocity u_j and the corresponding passive scalar θ can be written as

$$\frac{\partial u_j}{\partial t}+u_i\frac{\partial u_j}{\partial x_i}=-\frac{1}{\rho}\frac{\partial p}{\partial x_j}+\nu\frac{\partial^2 u_j}{\partial x_i\partial x_i}, \tag{2.1}$$

$$\frac{\partial u_j}{\partial x_j}=0, \tag{2.2}$$

$$\frac{\partial \theta}{\partial t}+u_i\frac{\partial \theta}{\partial x_i}=D\frac{\partial^2 \theta}{\partial x_i\partial x_i}. \tag{2.3}$$

Here ν and D are kinetic viscosity and the diffusivity for passive scalar, respectively. Eqs. (2.1)-(2.3) are solved in a cubic box of side $L_B=2\pi$. A standard pseudo-spectral algorithm is adopted with periodic boundary conditions in all three coordinates directions. The flow domain is discretized on $N^3=1024^3$ grid points, and $k_{\max}\eta$ is kept to be 1.5 to resolve the smallest scale motions of the velocity field, where $k_{\max}=\sqrt{2}N/3$ and η is the Kolmogorov length scale. The second-order Adams-Bashforth scheme is implemented

for temporal integration. A statistically steady state is obtained by using a low Fourier mode forcing for both the velocity and scalar fields, and a total of 20 snapshots are extracted to analyze the flow statistics. The Taylor Reynolds number is $R_\lambda=410$, defined as $R_\lambda=u_{\rm rms}\lambda/\nu$ with

$$u_{\rm rms}=\left(\frac{2}{3}\int E(k)\mathrm{d}k\right)^{1/2},\quad \lambda=\left(15\frac{u_{\rm rms}^2\nu}{\varepsilon}\right)^{1/2},\quad \varepsilon=2\nu\int_0^\infty k^2E(k)\mathrm{d}k. \tag{2.4}$$

Here $E(k)=\sum_{\boldsymbol{k}}|\boldsymbol{u}_F(\boldsymbol{k})|^2$, $k-0.5\leqslant|\boldsymbol{k}|<k+0.5$ is the spectrum of velocity field, where $\boldsymbol{u}_F(\boldsymbol{k})$ is the velocity vector in Fourier space at wavenumber $\boldsymbol{k}$. The spectrum for passive scalar field, denoted as $E_\theta(k)$, can be defined analogically. The Prandtl number ($Pr=\nu/D$) is chosen to be 0.7 to ensure adequate resolution for the scalar field.

An LES with 512^3 grid points is carried out to obtain the higher Reynolds number field, and the governing equations for the filtered velocity $\overline{u}_j$ and passive scalar $\overline{\theta}$ are

$$\frac{\partial\overline{u}_j}{\partial t}+\overline{u}_i\frac{\partial\overline{u}_j}{\partial x_i}=-\frac{1}{\overline{\rho}}\frac{\partial\overline{p}}{\partial x_j}+\nu\frac{\partial^2\overline{u}_j}{\partial x_i\partial x_i}-\frac{\partial\tau_{ij}}{\partial x_i}, \tag{2.5}$$

$$\frac{\partial\overline{u}_j}{\partial x_j}=0, \tag{2.6}$$

$$\frac{\partial\overline{\theta}}{\partial t}+\overline{u}_i\frac{\partial\overline{\theta}}{\partial x_i}=D\frac{\partial^2\overline{\theta}}{\partial x_i\partial x_i}-\frac{\partial\tau_{i\theta}}{\partial x_i}. \tag{2.7}$$

Eqs. (2.5)-(2.7) are solved with the same numerical method as the DNS. The small scale motions below the grid resolution (the LES filter width Δ) are modelled by the dynamic Clark model [43, 44], which can be written as

$$\tau_{ij}=-C_d\Delta^2\overline{S}\,\overline{S}_{ij}+\frac{1}{12}\Delta^2\frac{\partial\overline{u}_i}{\partial x_k}\frac{\partial\overline{u}_j}{\partial x_k}, \tag{2.8}$$

$$\tau_{i\theta}=-C_d^\theta\Delta^2\overline{S}\frac{\partial\overline{\theta}}{\partial x_i}+\frac{1}{12}\Delta^2\frac{\partial\overline{u}_i}{\partial x_j}\frac{\partial\overline{\theta}}{\partial x_j}, \tag{2.9}$$

where $\overline{S}_{ij}=(\partial\overline{u}_i/\partial\overline{x}_j+\partial\overline{u}_j/\partial\overline{x}_i)/2$ and $\overline{S}=(2\overline{S}_{ij}\overline{S}_{ij})^{1/2}$. The coefficients C_d and C_d^θ are determined dynamically with the least-squares approach:

$$C_d=\frac{\langle M_{ij}(L_{ij}-H_{ij})\rangle}{\langle M_{ij}M_{ij}\rangle},\quad C_d^\theta=\frac{\langle M_{i\theta}(L_{i\theta}-H_{i\theta})\rangle}{\langle M_{i\theta}M_{i\theta}\rangle}, \tag{2.10}$$

$$M_{ij}=-\hat{\Delta}^2\hat{\overline{S}}\,\hat{\overline{S}}_{ij}+\Delta^2\widehat{\overline{S}\overline{S}_{ij}},\quad L_{ij}=\widehat{\overline{u}_i\overline{u}_j}-\hat{\overline{u}}_i\hat{\overline{u}}_j,\quad H_{ij}=\frac{1}{12}\hat{\Delta}^2\frac{\partial\hat{\overline{u}}_i}{\partial x_k}\frac{\partial\hat{\overline{u}}_j}{\partial x_k}-\frac{1}{12}\Delta^2\widehat{\frac{\partial\overline{u}_i}{\partial x_k}\frac{\partial\overline{u}_j}{\partial x_k}}, \tag{2.11}$$

$$M_{i\theta}=-\hat{\Delta}^2\hat{\overline{S}}\frac{\partial\hat{\overline{\theta}}}{\partial x_i}+\Delta^2\widehat{\overline{S}\frac{\partial\overline{\theta}}{\partial x_i}},\quad L_{i\theta}=\widehat{\overline{u}_i\overline{\theta}}-\hat{\overline{u}}_i\hat{\overline{\theta}},\quad H_{i\theta}=\frac{1}{12}\hat{\Delta}^2\frac{\partial\hat{\overline{u}}_i}{\partial x_j}\frac{\partial\hat{\overline{\theta}}}{\partial x_j}-\frac{1}{12}\Delta^2\widehat{\frac{\partial\overline{u}_i}{\partial x_j}\frac{\partial\overline{\theta}}{\partial x_j}}. \tag{2.12}$$

The hat ($\widehat{\cdots}$) in Eqs. (2.11)-(2.12) denotes a test filter with filter width $\hat{\Delta}=2\Delta$.

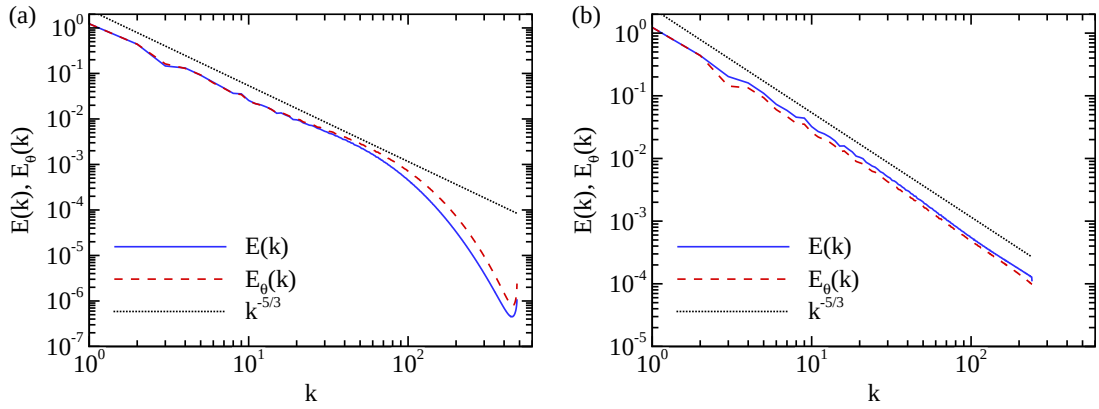

Figure 1: Spectra of velocity and passive scalar for (a) DNS field and (b) LES field.

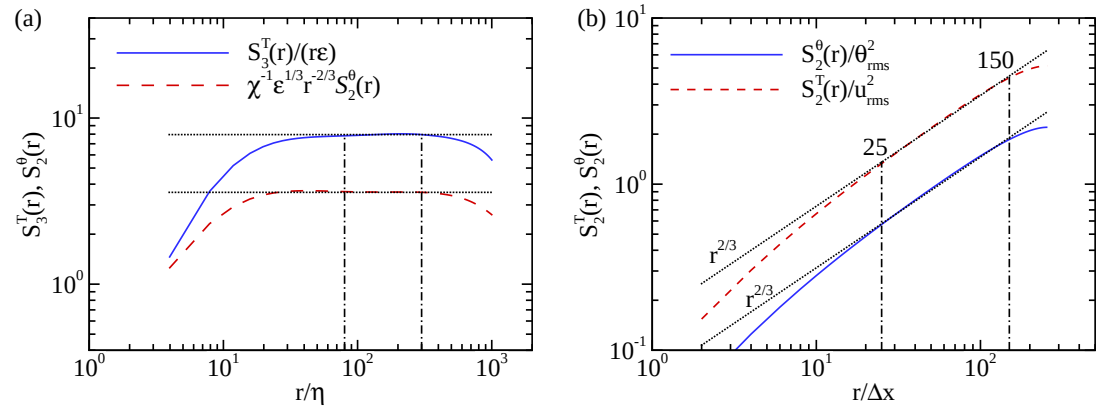

Figure 2: Inertial-range of the transverse velocity and passive scalar. (a) Normalized $S_3^T(r)$ and $S_2^\theta(r)$ of the DNS field. Here $\chi=2D\langle(\partial\theta/\partial x_i)^2\rangle$ is the dissipation for the passive scalar field; $\eta=(\nu^3/\varepsilon)^{1/4}$. (b) $S_2^T(r)$ and $S_2^\theta(r)$ of the LES field, normalized with the root-mean-square of velocity fluctuation $u_{\rm rms}$ and passive scalar fluctuation $\theta_{\rm rms}$, respectively.

Fig. 1 shows the spectra of velocity and passive scalar for both the DNS and LES fields. The Taylor Reynolds number of the LES field, estimated using Eq. (2.4) and the energy spectrum shown in Fig. 1(b), is about 8300, which is much larger than that of the DNS field. As a result, the $E(k)$ and $E_\theta(k)$ of the LES field have a longer range close to the $k^{-5/3}$ power-law than those of the DNS field. The normalized $S_3^T(r)$ and S_2^θ are plotted in Fig. 2(a), and plateaus can be clearly observed in the interval $80\lesssim r/\eta\lesssim 300$, which is selected as the inertial range for transverse velocity and passive scalar of the DNS field. The normalized second-order structure functions for velocity and passive scalar of the LES field are shown in Fig. 2(b). It is seen that both $S_2^T(r)$ and $S_2^\theta(r)$ fit the $r^{2/3}$ scaling-law fairly well in the interval $25\lesssim r/\Delta x\lesssim 150$ (Δx is the smallest grid width), which can be selected as the inertial range of the LES field in the following analysis.

2.2 Fractal Brownian motion

An FBM series $X(t)$ with $N=2\times10^8$ samples is generated using the subroutine `wfbm` in MATLAB, which employs the algorithm of Abry and Sellan [45]. The Hurst parameter is chosen to be $H=1/3$, such that the scaling of the structure function $S_p(\tau)$ can reproduce the K41 law, where $S_p(\tau)=\langle|X(t+\tau/2)-X(t-\tau/2)|^p\rangle$. It is clearly seen from Fig. 3, as expected, that the scaling relation of the FBM series satisfies $S_p(\tau)\sim\tau^{\zeta_p}$ with $\zeta_p=p/3$ fairly well for $p=1\sim10$ at all scales.

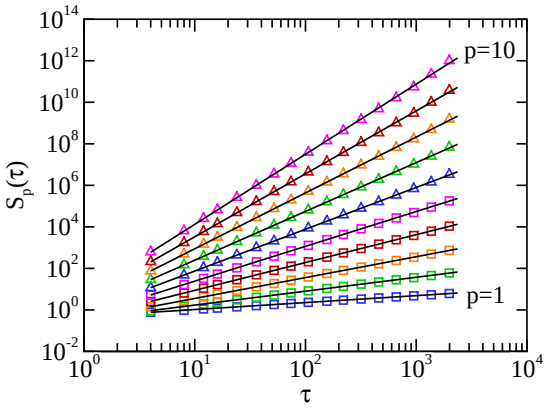

Figure 3: The structure functions of the FBM series. The Hurst parameter is chosen to be $H=1/3$. Solid lines represent the scaling-laws of $\tau^{p/3}$.

2.3 Oscillation structure classification

The oscillation structure classification method is based on the local zero-crossing, which is a modification of the classical zero-crossing that has been studied extensively [46–51]. This OS classification method can be employed in any fluctuation field ϕ, where ϕ can be either the velocity or passive scalar fluctuations. Since the turbulence signal contains both large-scale and small-scale structures, the dissipative-scale motions may serve as noise to the identification of inertial-range structures. We first apply a low-pass filter on ϕ to get the coarse-grained $\tilde{\phi}(x)$ and define the local mean $\tilde{\phi}_r(x)$ as $\tilde{\phi}_r(x)=\frac{1}{r}\int_{x-r/2}^{x+r/2}\tilde{\phi}(y)\mathrm{d}y$. In the present study, the Gaussian low-pass filter with filter width αr is used, where α depends on the ratio of the smallest/largest inertial-range lengths, and should be properly chosen to remove the effect of small-scale motions in the inertial range. Here, α is chosen to be $1/8$ for both the DNS and LES fields; see Appendix for detailed discussion about the effect of filter width. Then we denote $N_r(\tilde{\phi})$ as the number of the zero points of $\tilde{\phi}(x)-\tilde{\phi}_r$ in the interval $[x-r/2,x+r/2]$ (local zero crossings). The use of $\tilde{\phi}_r$ instead of the global mean value $\langle\phi\rangle$ can avoid the influence of large-scale motions on the local structures. As a result, the oscillation structures at the characteristic scale r can be discerned by counting $N_r(\tilde{\phi})$ in the interval $[x-r/2,x+r/2]$. We define the oscillation structure classification

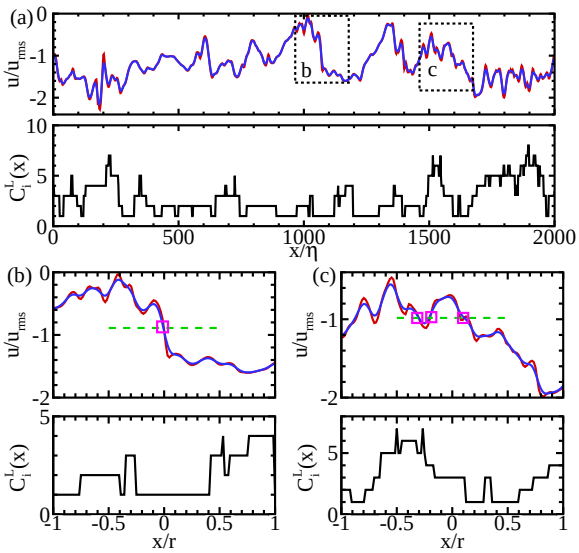

Figure 4: The oscillation structure classification for the DNS velocity field at $R_\lambda = 410$ and $r = 128\eta$. (a) Upper: a segment of original velocity (red line) and filtered velocity (blue line). Lower: the corresponding OS subclasses; (b) The detailed illustration of $u(x)$, $\tilde{u}(x)$ and $C_i^L(x)$ at the neighbor of position b in (a); (c) The detailed illustration of $u(x)$, $\tilde{u}(x)$ and $C_i^L(x)$ at the neighbor of position c in (a). The dashed lines represent $\tilde{u}_r$ at $x=0$. Symbols denote the local zero-crossings.

and the subclasses for ϕ as

$$C_i(r) \equiv \{i \,|\, N_r(\tilde{\phi}(x)) = i\}. \tag{2.13}$$

We use C_i^L, C_i^T and C_i^θ to denote the OS subclasses for the longitudinal velocity, transverse velocity and passive scalar, respectively. Fig. 4(a) shows a segment of longitudinal velocity component before and after the filtered process along x direction of a DNS field, as well as the corresponding OS subclasses. The $u(x)$, $\tilde{u}(x)$ and $C_i^L(x)$ around position b and c are shown in details in Fig. 4(b) and Fig. 4(c). When $C_i^L = 1$, it usually means that a large drop-off structure (ramp-cliff) is formed, as shown in Fig. 4(b). When $C_i^L = 3$, a zigzag structure exist in the interval $[x-r/2, x+r/2]$ as shown in Fig. 4(c). Obviously the larger the value of C_i^L is, the faster the structure oscillates and more local zero-crossings are recognized. The relation between the value of C_i and the corresponding oscillation structure is the same for the transverse velocity and passive scalar.

3 Results

3.1 Intermittency and oscillation structures

To study the connection between the inertial-range intermittence and oscillation structures, we first apply the OS classification on the transverse velocity of DNS and LES fields and check the general statistics of the OS subclasses. Fig. 5(a) shows the probability den-

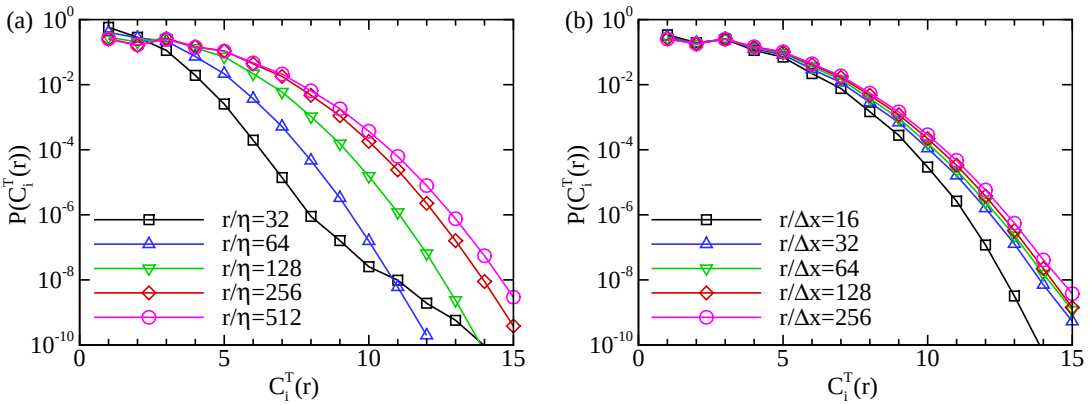

Figure 5: The probability density functions of oscillation structure subclasses for transverse velocity at different cover lengths r. (a) The DNS field. (b) The LES field on 512^3 grid points.

sity functions (PDFs) of OS subclasses in the DNS field. It is seen that when $r/\eta \leqslant 64$, the PDFs depend on r strongly. In the range $r/\eta \geqslant 128$, the PDFs of the $C_1^T \sim C_5^T$ subclasses can nearly collapse with each other at different cover lengths, illustrating that the PDFs of these five OS subclasses are scale-invariant at these scales. The faster oscillating subclasses, such as $C_6^T \sim C_{15}^T$, show a slower convergent rate to an asymptotic distribution. We postulate that if the flow field had a higher Reynolds number and a longer inertial range, the scale-invariant feather of $P(C_i^T(r))$ could be satisfied better. This conjecture is verified in the LES field, and the corresponding PDFs of $C_i^T(r)$ are shown in Fig. 5(b). It is observed that the PDFs at different r can collapse with each other fairly well, except for the $r{=}16\Delta x$ case which might be affected by the subgrid-scale model. A similar result has been reported in the companion paper [40], which is based on the statistics of longitudinal velocity from DNS and experimental measurement in an atmosphere boundary layer at $R_\lambda = 19500$. These results indicate that when the slower OS subclasses ($C_1^T \sim C_5^T$) are considered, which occupy the majority of the flow field, the statistical scale-invariance can sustain for transverse velocity at both moderate and high Reynolds numbers; and $P(C_i^T(r))$ is independent of r in high Reynolds number field for all OS subclasses.

The next step is to study the inertial-range intermittent level in each OS subclass by investigating the scalings of conditional structure functions $S_{p,i}^T$ on different C_i^T subclasses: $S_p^T(r)|C_i^T(r) \equiv \langle |\delta_r v|^p | C_i^T(r) \rangle$. Due to the limited length of the inertial range, the extended-self similarity (ESS) [52] is utilized to estimate the relative scalings, and the ESSs of the C_1^T and C_7^T subclasses are shown in Fig. 6. It is seen that the relative scaling law, $S_{p,i}^T \sim (S_{3,i}^T)^{\zeta_{p,i}^E}$, can be satisfied fairly well in both subclasses. This well-matched relationship is also observed in other subclasses and the results are not shown here to avoid redundancy. The $(\ln S_{p,i}^T, \ln S_{3,i}^T)$ curves are least squares fitted with straight lines to extract the slope $\zeta_{p,i}^E$s, and we fit the $(\ln S_{3,i}^T, \ln r)$ curves in different subclasses using the same approach to get the absolute scaling $\zeta_{3,i}^T$s. The scaling exponents $\zeta_{p,i}^T$s for $p \neq 3$ are obtained by $\zeta_{p,i}^T = \zeta_{3,i}^T \zeta_{p,i}^E$,

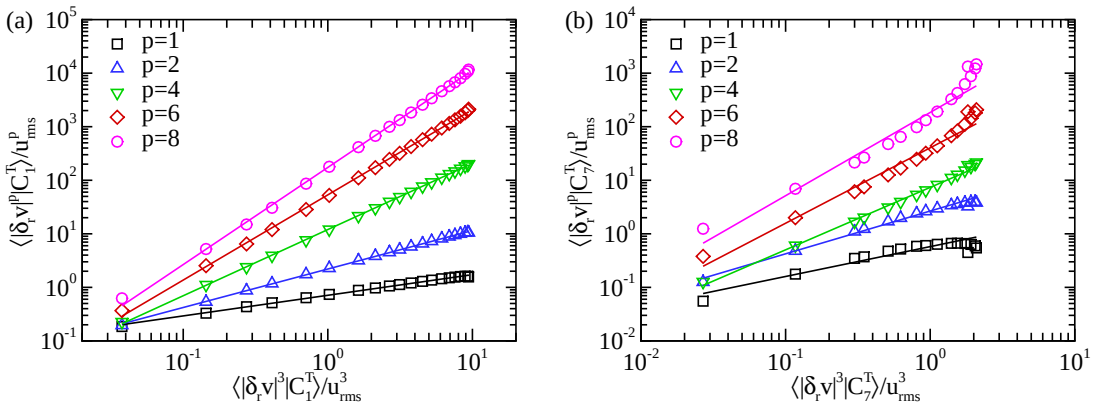

Figure 6: The extended self similarity for transverse structure functions of DNS field in different transverse OS subclasses, including the least squares fits to measure the relative scalings (solid lines). Data symbols and lines are shifted vertically by different amounts for better recognition. (a) C_1^T subclass; (b) C_7^T subclass.

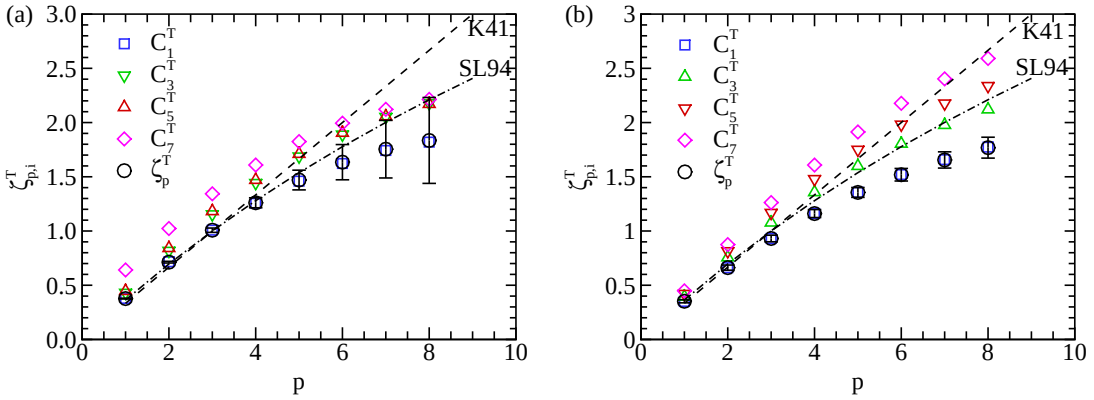

Figure 7: The absolute scalings of transverse structure functions in each transverse OS subclass as well as ζ_p^T of the overall field for (a) DNS field and (b) LES field on 512^3 grid points. The error bar denotes for the standard derivation of ζ_p^T of time average. Dashed lines (K41) represent the scaling $\zeta_p = p/3$ predicted by Kolmogorov 1941 theory. Dash-dotted lines (SL94) represent the scaling $\zeta_p = p/9+2[1-(2/3)^{p/3}]$ predicted by She and Leveque [18].

and they are shown in Fig. 7(a). The scaling exponent of $S_p^T(r)$ of the overall field (denoted by ζ_p^T) is also plotted in the same figure, and it is found that for $p=1\sim8$, ζ_p^T is approximately equal to $\zeta_{p,1}^T$, which is the minimum of scalings in all the OS subclasses. This demonstrates that the inertial-range intermittency of the overall field is determined by the most intermittent oscillating structure, i.e., the C_1^T OS subclass. The relation $\zeta_p^T = \zeta_{p,1}^T$ can also be deduced analytically provided the statistical invariance of the PDFs of $C_i^T(r)$, as presented in details in the companion paper [40], and will not be repeated here. The absolute scalings of transverse structure functions in different OS subclasses of the LES

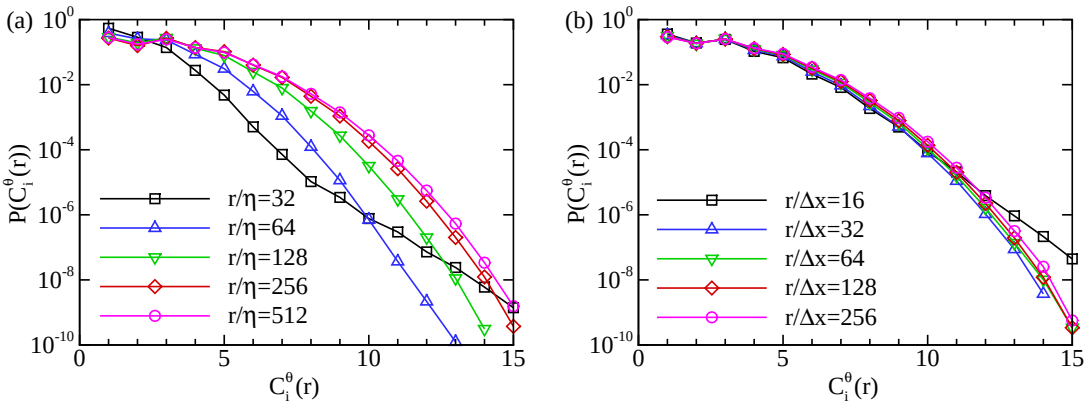

Figure 8: The probability density functions of oscillation structure subclasses for passive scalar at different cover lengths r for (a) the DNS field and (b) the LES field on 512^3 grid points.

field are shown in Fig. 7(b), and the results are very close to that of the DNS field. To check the applicability of the LES approach, we performed another LES with 128^3 grid points and the same flow parameters of the DNS field, and the corresponding results are comparable to those of the DNS field (results are not shown here). It indicates that the results obtained in the LES field of 512^3 grid points are not trivial. We infer that the relation between the oscillation structures and the inertial-range intermittency for transverse velocity is valid for both moderate and high Reynolds number field.

The routine of classification based on oscillation structures and conditional statistics is also applied to passive scalar field. Fig. 8(a) shows that the PDFs of C_i^θ has an asymptotic form as r becomes larger in the inertial range at moderate Reynodes number. At high-Reynoldes number, all the $P(C_i^\theta(r))$s can collapse very well as shown in Fig. 8(b). The intermittent levels of different OS subclasses are also investigated in the passive scalar field. We study the scaling-law of structure function conditional on different C_i^θ subclasses: $S_{p,i}^\theta \sim r^{\xi_{p,i}}$, where $S_p^\theta(r)|C_i^\theta(r) = \langle|\delta_r\theta|^p|C_i^\theta(r)\rangle$. The ESS approach for obtaining $\zeta_{p,i}^T$ is employed to calculate the $\xi_{p,i}$, and the result is shown in Fig. 9. It is seen that the relation $\xi_p = \xi_{p,1}$ can be satisfied in both DNS and LES fields, which is also consistent with the results of the velocity field presented in the companion paper [40] and Fig. 7.

One manifestation of inertial-range intermittency is the non-Gaussian behavior of velocity increment in the inertial-range scale. Fig. 4 gives a qualitative illustration that the C_1^T subclass contains the large jumps of velocity fluctuations, which are usually contained in the non-Gaussian tail part of PDF for $\delta_r v$. This property for C_1^T subclass is verified in a more quantitative way in Fig. 10(a), which plots the joint PDF of the transverse velocity increment and OS subclasses (denoted by $P(\delta_r v, C_i^T)$) as well as the PDF of $\delta_r v$ of the overall field (denoted by $P(\delta_r v)$) when $r = 128\eta$, and we have $\sum_i P(\delta_r v, C_i^T) = P(\delta_r v)$. It is seen that the probability of $\delta_r v$ in the C_1^T subclass has the longest tails on both the positive and negative sides, indicating that the velocity increments with large values, such

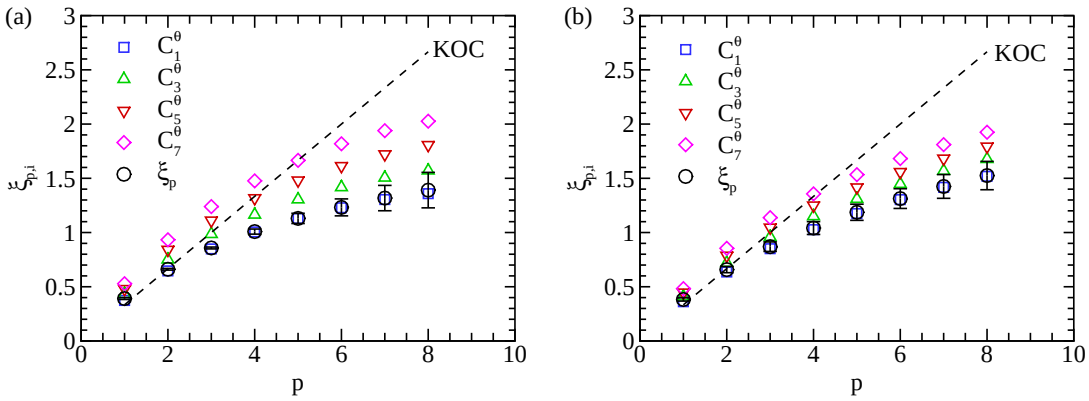

Figure 9: The absolute scalings of structure functions of passive scalar field in each OS subclass as well as ξ_p of the overall field for (a) DNS field and (b) LES field on 512^3 grid points. The error bar denotes for the standard derivation of ξ_p of time average. Dashed lines (KOC) represent the scaling $\xi_p = p/3$ predicted by KOC theory.

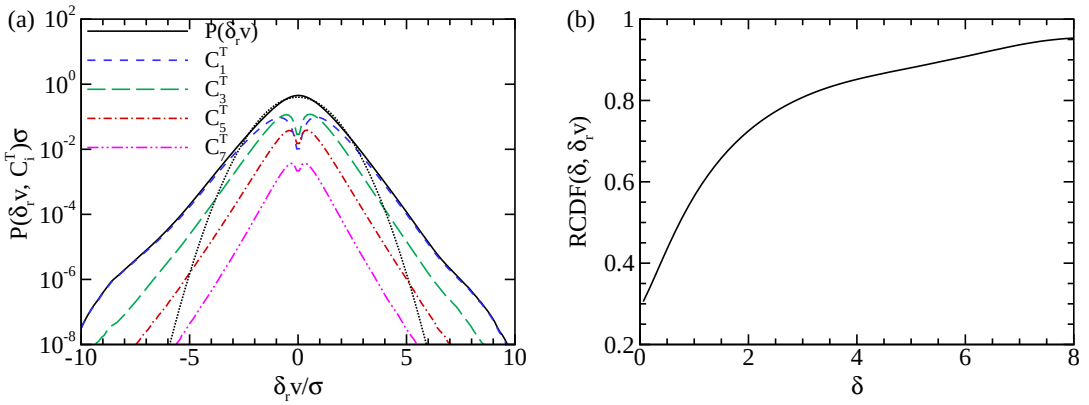

Figure 10: (a) The joint PDF of the transverse velocity increment and OS subclasses as well as $P(\delta_r v)$ of the overall field at $r = 128\eta$. σ is the r.m.s of $\delta_r v$. The dotted line is the Gaussian distribution. (b) The RCDF of the transverse velocity increment.

as $\delta_r v/\sigma > 3$, have the highest probability in the C_1^T subclass. Meanwhile, it is remarkable that the tails of $P(\delta_r v, C_1^T)$ are almost overlap with $P(\delta_r v)$ of the overall field, while other OS subclasses have much smaller probability at the tail parts. To measure the contribution of C_1^T subclass more preciously, we define the ratio of cumulative probability function (RCDF) of $\delta_r v$ in C_1^T subclass and the overall field as

$$\mathrm{RCDF}(\delta,\, \delta_r v) = \frac{P(|\delta_r v|/\sigma > \delta, C_1^T)}{P(|\delta_r v|/\sigma > \delta)}, \tag{3.1}$$

and plot it in Fig. 10(b). It is seen that when $\delta = 3$, RCDF $= 0.84$, meaning that more than 80% of regions with $|\delta_r v|/\sigma > 3$ are captured by the C_1^T subclass. And this ratio can exceed 90% when the events of $|\delta_r v|/\sigma > 5.75$ are considered. It shows that the extreme velocity

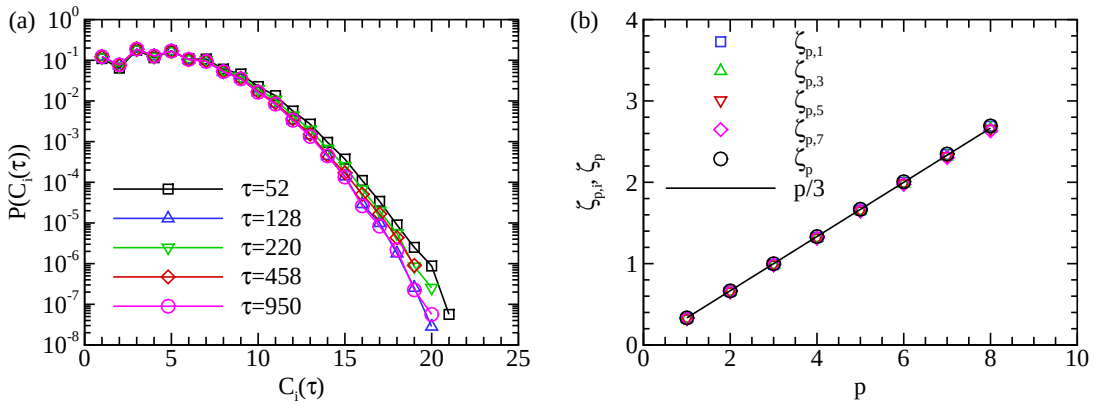

Figure 11: (a) The probability density functions of oscillation structure subclasses of the FBM series. (b) The scalings of $S_p(\tau)|C_i$ and $S_p(\tau)$ of the FBM series.

increments that cause the non-Gaussian part of the PDF locate mostly in the C_1^T subclass regions. The results of the passive scalar field are similar to those of the velocity field, and will not be shown here.

In contrast to the turbulent fields which have the intermittent feature, the fractal Brownian motion is a self-similar Gaussian process without intermittency at all scales. The PDFs of $C_i(\tau)$ from the FBM series at different scales are shown in Fig. 11(a). It is seen that $P(C_i(\tau))$ is independent of τ. Thus the scale-invariant feature of the PDFs of OS subclasses can be satisfied in the FBM field for a wide range of scales, which is also a reflection of the self-similarity. The scalings of structure functions in each OS subclasses and the overall FBM series are shown in Fig. 11(b). It is clear that $\zeta_{p,i}=\zeta_p=p/3$ for all $i=1\sim 7$. This demonstrates that the OS classification will not induce any artificial intermittent structure.

3.2 Topology and oscillation structures

The topological structure of the local streamlines is determined by the eigenvalues (denoted as λ_i, $i=1,2,3$) of the velocity gradient tensor $A_{ij}=\partial u_i/\partial x_j$, which satisfy

$$\lambda_i^3+P\lambda_i^2+Q\lambda_i+R=0, \tag{3.2}$$

where P, Q and R are the first, second and third invariants of the tensor A_{ij}, respectively, and they are given by

$$P=-S_{ii}, \tag{3.3}$$

$$Q=\frac{1}{2}(P^2-S_{ij}S_{ij}+\Omega_{ij}\Omega_{ij}), \tag{3.4}$$

$$R=\frac{1}{3}(-P^3+3PQ-S_{ij}S_{jk}S_{ki}-3\Omega_{ij}\Omega_{jk}S_{ki}), \tag{3.5}$$

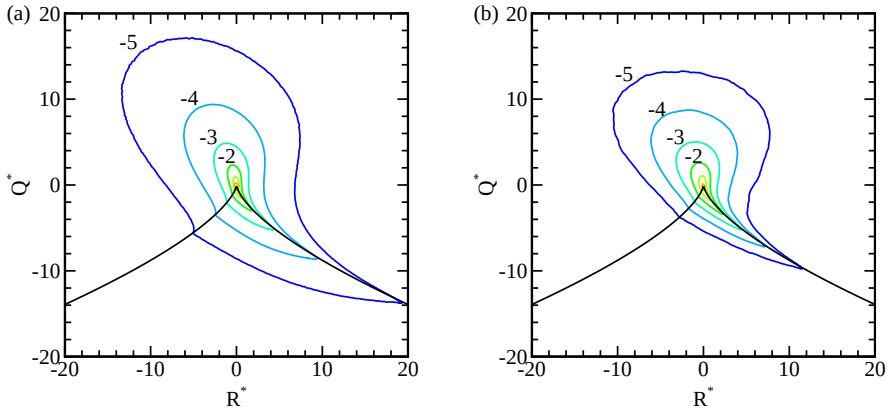

Figure 12: Isocontour lines of $\log_{10}P(Q^*,R^*)$. Five contour lines at -1, -2, -3, -4 and -5 are shown for (a) the original velocity field and (b) the filtered velocity field. Black curves in (a) and (b) are for $27R^{*2}+4Q^{*3}=0$.

and $S_{ij}=(A_{ij}+A_{ji})/2$, $\Omega_{ij}=(A_{ij}-A_{ji})/2$. In the incompressible field, $P=0$, and the discriminant $\Delta(\boldsymbol{u})$ of Eq. (3.2) is

$$\Delta(\boldsymbol{u})=27R^2+4Q^3. \tag{3.6}$$

According to Chong et al. [41], if $\Delta(\boldsymbol{u})<0$, the three eigenvalue of A_{ij} are all real, corresponding to the non-focal region (the saddle region); On the other hand, when $\Delta(\boldsymbol{u})>0$, only one eigenvalue is real and the other two ones are complex conjugate pairs, corresponding to the focal region (the vortex region).

The joint PDF of (Q,R) of the DNS field at $R_\lambda=410$ is shown in Fig. 12(a), where $Q^*=Q/\Omega^3$, $R^*=R/\Omega^2$ and $\Omega=|\nabla\times\boldsymbol{u}|/\sqrt{2}$. The teardrop shape of the joint PDF of (Q,R) is consistent with the results reported by Martin et al. [53] and Meneveau [54]. However, the classic topological analysis can only discern the flow patterns at very small scales. To analyze the inertial-range motions, the DNS field is filtered by a low-pass filter with width $\overline{\Delta}=r$, where r is the cover length scale used in the OS classification, and $(Q(\overline{\boldsymbol{u}}),R(\overline{\boldsymbol{u}}))$ of the filtered velocity field $\overline{\boldsymbol{u}}$ is analyzed to study the flow topologies at the scale r. The joint PDF of $(Q(\overline{\boldsymbol{u}}),R(\overline{\boldsymbol{u}}))$ at $r=128\eta$ is shown in Fig. 12(b), where $Q^*=Q(\overline{\boldsymbol{u}})/\overline{\Omega}^3$, $R^*=R(\overline{\boldsymbol{u}})/\overline{\Omega}^2$, $\overline{\Omega}=|\nabla\times\overline{\boldsymbol{u}}|/\sqrt{2}$. It is seen that the joint PDF of $(Q(\overline{\boldsymbol{u}}),R(\overline{\boldsymbol{u}}))$ still has the teardrop shape, but covers a smaller area.

Since the topological analysis is a three-dimensional (3D) classification method and the OS subclasses for different directions are weakly correlated, the one-dimensional OS subclasses $C_i(u_1)$, $C_i(u_2)$ and $C_i(u_3)$ are summed as $C_{3d}=C_i(u_1)+C_i(u_2)+C_i(u_3)$ to be a measure of 3D oscillation structures. A special emphasis should be placed on positions where $C_{3d}=3$, since it means at these positions all the u_1, u_2 and u_3 belong to the C_1 subclass. The topological characteristics in the $C^L_{3d}=3$ subdomains of the longitudinal velocity is investigated and the joint PDF of $(Q(\overline{\boldsymbol{u}}),R(\overline{\boldsymbol{u}}))$ is shown in Fig. 13(a). It is seen that $P(Q(\overline{\boldsymbol{u}}),R(\overline{\boldsymbol{u}}))_{C^L_{3d}=3}$ has a smaller probability in the $Q(\overline{\boldsymbol{u}})>0,R(\overline{\boldsymbol{u}})>0$ region, and a

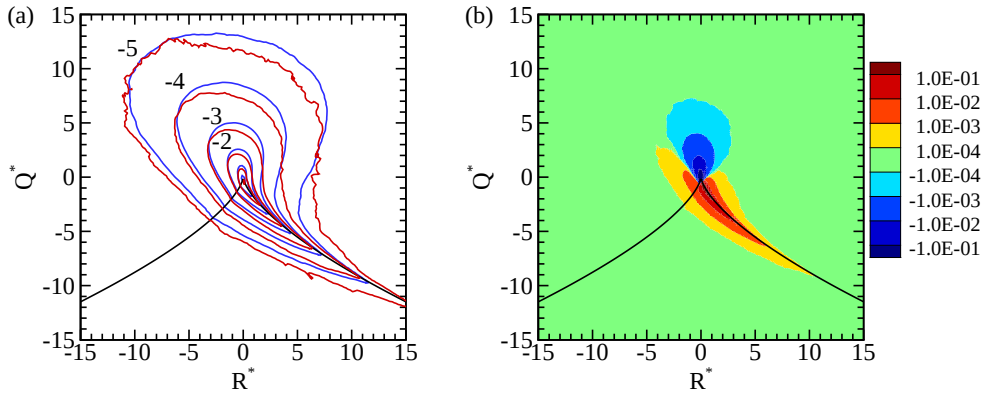

Figure 13: The local flow topology related to the OS subclass of longitudinal velocity at $r=128\eta$. (a) Isocontour lines of $\log_{10}P(Q^*,R^*)$ for the filtered velocity in the $C_{3d}=3$ subdomains (the red lines) and the overall field (the blue lines). Five contour lines at -1, -2, -3, -4 and -5 are shown; (b) Contour of $P(Q^*,R^*)_{C_{3d}^L=3}-P(Q^*,R^*)$. Black curves in (a) and (b) are for $\Delta(\overline{\boldsymbol{u}})=27R^{*2}+4Q^{*3}=0$.

significant larger probability around the right branch of the $\Delta(\overline{\boldsymbol{u}})=0$ curve compared with the joint PDF of $(Q(\overline{\boldsymbol{u}}),R(\overline{\boldsymbol{u}}))$ of the overall field. The difference between the joint PDF of $(Q(\overline{\boldsymbol{u}}),R(\overline{\boldsymbol{u}}))$ conditional on the $C_{3d}^L=3$ subdomains and that of the overall field, i.e. $P(Q(\overline{\boldsymbol{u}}),R(\overline{\boldsymbol{u}}))_{C_{3d}^L=3}-P(Q(\overline{\boldsymbol{u}}),R(\overline{\boldsymbol{u}}))$, is shown in Fig. 13(b). It is seen that the difference of the two joint PDFs has a large area of positive value around the right branch of $\Delta(\overline{\boldsymbol{u}})=0$ curve as well as a large area of negative value in the $Q(\overline{\boldsymbol{u}})>0$ region. This illustrates that $C_{3d}^L=3$ subdomains have a higher probability to lay in the saddle or degenerated saddle regions and a lower probability in the vortex-dominated region.

The topological analysis is also combined with the OS classification of the transverse velocity. Since each velocity component have two transverse OS subclass, we define $\overline{C_i^T}$ for velocity component u_k as

$$\overline{C_i^T}(u_k)=\min\{C_i^T(r_{j_1},u_k),C_i^T(r_{j_2},u_k)\},\quad j_1\neq k,j_2\neq k,\quad k=1,2,3, \tag{3.7}$$

and define the measure of 3D transverse OS as

$$C_{3d}^T=\overline{C_i^T}(u_1)+\overline{C_i^T}(u_2)+\overline{C_i^T}(u_3). \tag{3.8}$$

The joint PDF of $(Q(\overline{\boldsymbol{u}}),R(\overline{\boldsymbol{u}}))$ conditional on the $C_{3d}^T=3$ subdomains is shown in Fig. 14(a). It is seen that the $C_{3d}^T=3$ subdomains have a much larger probability for the vortex region than the overall field, while the probabilities for the saddle region are almost the same. The difference between the joint PDFs of $(Q(\overline{\boldsymbol{u}}),R(\overline{\boldsymbol{u}}))$ conditional on the $C_{3d}^T=3$ subdomains and that of the overall field, i.e. $P(Q(\overline{\boldsymbol{u}}),R(\overline{\boldsymbol{u}}))_{C_{3d}^T=3}-P(Q(\overline{\boldsymbol{u}}),R(\overline{\boldsymbol{u}}))$, is shown in Fig. 14(b). It is seen that the difference of two joint PDFs has a large positive area in the $Q(\overline{\boldsymbol{u}})>0$ region, and it also has a small portion of positive value around the right branch of $\Delta(\overline{\boldsymbol{u}})=0$ curve. The negative value for the difference of two joint PDFs

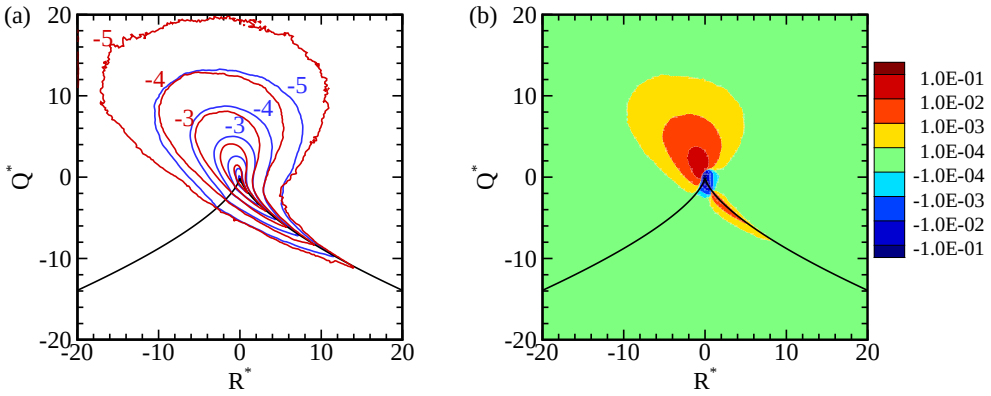

Figure 14: The local flow topology related to the OS subclass of transverse velocity at $r=128\eta$. (a) Isocontour lines of $\log_{10}P(Q^*,R^*)$ for the filtered velocity in the $C_{3d}^T=3$ subdomains (the red lines) and the overall field (the blue lines). Five contour lines at -1, -2, -3, -4 and -5 are shown. (b) Contour of $P(Q^*,R^*)_{C_{3d}^T=3}-P(Q^*,R^*)$. Black curves in (a) and (b) are for $\Delta(\overline{\boldsymbol{u}})=27R^{*2}+4Q^{*3}=0$.

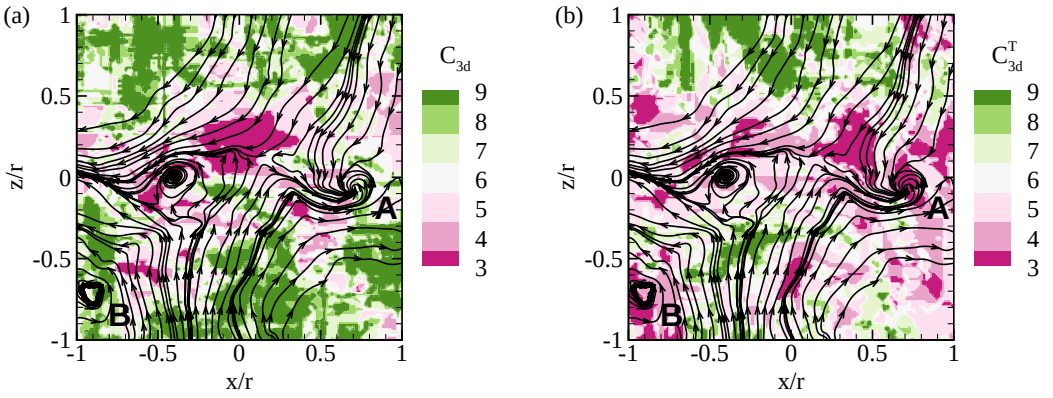

Figure 15: The two-dimensional streamlines for (u_1,u_3) and the OS subclass distribution at $r=128\eta$ on a selected (x,z) plane around a saddle point. The contour is (a) C_{3d}^L and (b) C_{3d}^T.

is around the $(Q(\overline{\boldsymbol{u}}),R(\overline{\boldsymbol{u}}))\to(0,0)$ region, which means that the weak rotation/strain regions are less probable to produce a C_1 subclass for the transverse velocity.

One typical saddle point with its surrounding flow structures extracted from the DNS field is shown in Fig. 15, where the contours of C_{3d}^L and C_{3d}^T are shown as the backgrounds in panel (a) and (b), respectively. The longitudinal velocity components in both the x and z directions change their signs when they cross the saddle point, and large jumps (or the cliff structure with $C_{3d}^L=3$) can be observed near the saddle point at the center of the figure. Meanwhile, C_{3d}^L is usually larger than 3 near the vortex structures. On the other hand, as shown in Fig. 15(b), $C_{3d}^T=3$ regions are mostly at the neighbourhood or center of vortex structures (A and B), since the transverse velocity components change their

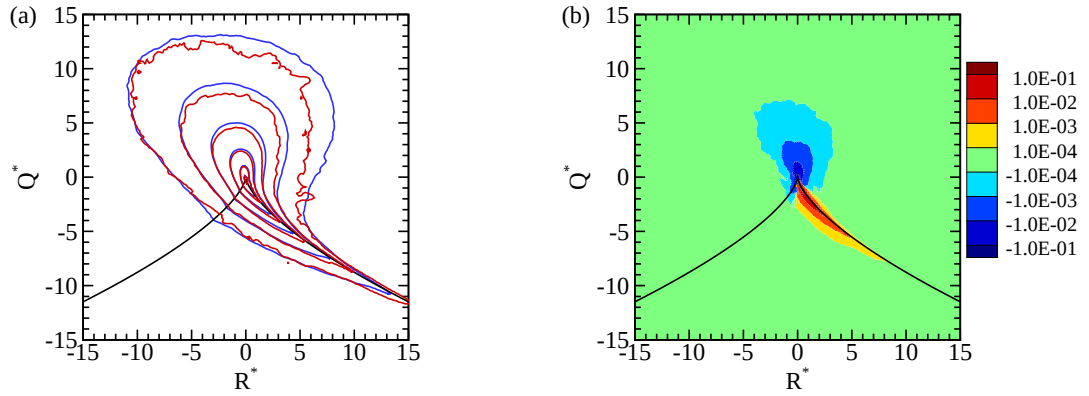

Figure 16: The local flow topology related to the OS subclass of passive scalar at $r=128\eta$. (a) Isocontour lines of $\log_{10}P(Q^*,R^*)$ for the filtered velocity in the $C_{3d}^{\theta}=3$ subdomains (the red lines) and the overall field (the blue lines). Five contour lines at -1, -2, -3, -4 and -5 are shown. (b) Contour of $P(Q^*,R^*)_{C_{3d}^{\theta}=3}-P(Q^*,R^*)$. Black curves in (a) and (b) are for $\Delta(\overline{\boldsymbol{u}})=27R^{*2}+4Q^{*3}=0$.

signs when they cross the center of a vortex. These results show that the intermittency of longitudinal structure function is related to the strain dominated region (the saddle region), while that of transverse structure function is related to the rotation dominated region (the vortex region). Our findings are consistent with the conclusions of Chen et al. [19] and Boratav and Pelz [33], and we would like to emphasize that the relation between the intermittency and the flow structures can be illuminated more clearly by our OS classification approach.

The topological analysis is also applied on the passive scalar field. We define the three-dimensional OS subclass for passive scalar as $C_{3d}^{\theta}=C_i^{\theta}(r_1)+C_i^{\theta}(r_2)+C_i^{\theta}(r_3)$, where $C_i^{\theta}(r_1)$, $C_i^{\theta}(r_2)$ and $C_i^{\theta}(r_3)$ are one-dimensional OS subclasses in x, y and z directions, respectively. The joint PDF of $(Q(\overline{\boldsymbol{u}}),R(\overline{\boldsymbol{u}}))$ of the $C_{3d}^{\theta}=3$ subdomains of the passive scalar is shown in Fig. 16(a). It has a similar behavior as the joint PDF of $(Q(\overline{\boldsymbol{u}}),R(\overline{\boldsymbol{u}}))$ in $C_{3d}^{L}=3$ subdomains of the longitudinal velocity, which can be seen more clearly from Fig. 16(b), that a smaller probability exists in the $Q(\overline{\boldsymbol{u}})>0$ region, and a larger probability exhibits around the right branch of the $\Delta(\overline{\boldsymbol{u}})=0$ curve. To further demonstrate the relation between the passive scalar structure and flow pattern of velocity field, we show the distribution of C_{3d}^{θ} and $\theta/\theta_{\rm rms}$ in Fig. 17(a) and (b) at the same flow region as that of Fig. 15. It is seen that a $C_{3d}^{\theta}=3$ area exists near the saddle point. A sharp front of passive scalar field is found near the $z=0$ line, and it passes two counter-rotating vortexes located at A and B. It has been reported by Antonia et al. [55] and Holzer and Siggia [39] that when a mean gradient is imposed on the passive scalar field, a scalar front (ramp-cliff structure) will occur at the diverging separatrix formed between two counter-rotating flowing structures. Our flow visualization clearly illustrates this physical picture, and shows that this relation between the passive scalar fonts and saddles of velocity field also exists in isotropic scalar field.

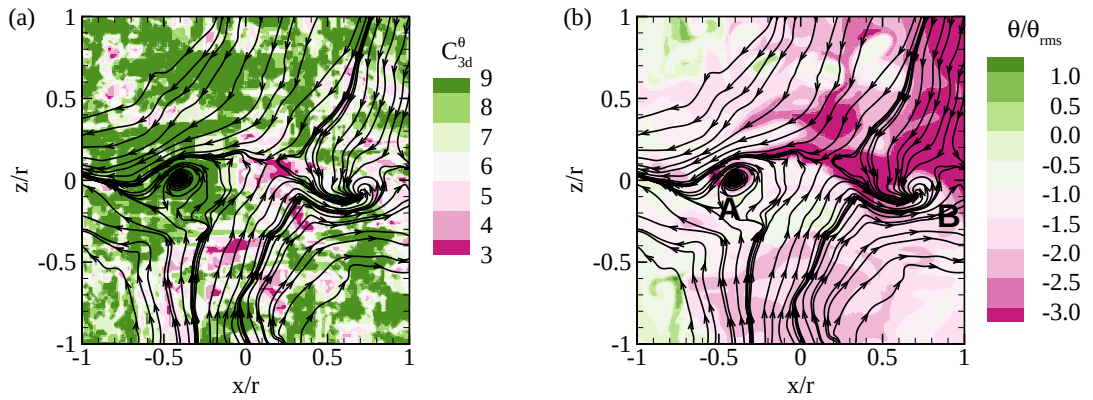

Figure 17: The two-dimensional streamlines for (u_1,u_3) and the OS subclass distribution and fluctuation of passive scalar at $r=128\eta$ on a selected (x,z) plane around a saddle point. The contour is (a) C^{θ}_{3d} and (b) $\theta/\theta_{\rm rms}$.

4 Summary

In this paper, we extend the oscillation structure classification method and conditional statistics tool developed in the longitudinal velocity to the transverse velocity, passive scalar field and the fractal Brownian motion. Flow fields obtained by DNS and LES are used to verify the relation between oscillation structure and inertial-range intermittency in moderate and high Reynolds number fields. We find that the probability of OS subclasses are scale-invariant in the inertial range at high Reynolds number for transverse velocity and passive scalar. Meanwhile, the inertial-range intermittency for the transverse velocity and passive scalar are both determined by the OS subclass with only one local zero-crossing. This OS subclass captures most positions with large increments which cause non-Gaussian PDFs of $\delta_r v$ and $\delta_r\theta$. These results are consistent with the findings about the essence of the inertial-range intermittence for the longitudinal velocity. Meanwhile, by examination on fractal Brownian motion field, we also prove that our OS classification method is physical and will not introduce any artificial intermittent structure.

The topological approach based on the distribution of the invariants for the filtered velocity gradient tensor at inertial range is combined with the oscillation structure classification. We construct the measure for three-dimensional oscillation structures using one-dimensional OS subclasses, and investigate the dominating topological feature of the most intermittent subdomains in both the velocity and passive scalar field. It is found that the most intermittent subdomains for the longitudinal velocity tend to lay at the saddle region, while those for the transverse velocity tend to locate at the vortex-dominated region. Meanwhile, the connection between the intermittency of passive scalar and the saddles of velocity field is also confirmed in our study.

Acknowledgments

The authors benefit much from the discussions with Dr. Jianchun Wang and Prof. Weidong Su. This work was supported by the National Science Foundation of China (NSFC Grant Nos. 11221061, 11302006 and 91130001). The simulations were done on the TH-1A super computer in Tianjin, China.

Appendix

A proper filter width plays an important role to extract the statistical scale-invariant property for oscillations structures, i.e. to ensure the precondition $P(C_i) = P(C_i(r))$, which results in $\zeta_p = \zeta_{p,1}$. This relation can be deduced analytically, which has been addressed in the companion paper [40] and will not be repeated here. In the following we will show the role of filter process in the numerical approach.

Take the passive scalar field obtained by DNS as an example. We consider three different filter widths, i.e. $\Delta = r/4$, $r/8$ and $r/16$, and plot the results in Figs. 18-19 (the results of $\Delta = r/8$ has been presented in Fig. 8 and Fig. 9). When $\Delta = r/4$ and $\Delta = r/8$, the PDFs of $C_i^\theta(r)$ can converge in the inertial range, and the relation $\xi_{p,1} \approx \xi_p$ can be satisfied fairly well under both filter widths; when $\Delta = r/16$, the PDFs of $C_i^\theta(r)$ exhibit a poorer convergent property and the diversity between $\xi_{p,1}$ and ξ_p is larger, since too much dissipative-scale motions are retained in the filtered signal.

If a fixed filter width Δ is used, as the cover length r becomes larger, the motions close to Δ are more likely to be the noise-like structures. Fig. 20(a) shows the PDFs of $C_i^\theta(r)$ for a fixed filter width $\Delta = 16\eta$. It is seen that the PDFs show little scale-similarity even for inertial-range scales. The corresponding scalings of structure functions in C_1^θ

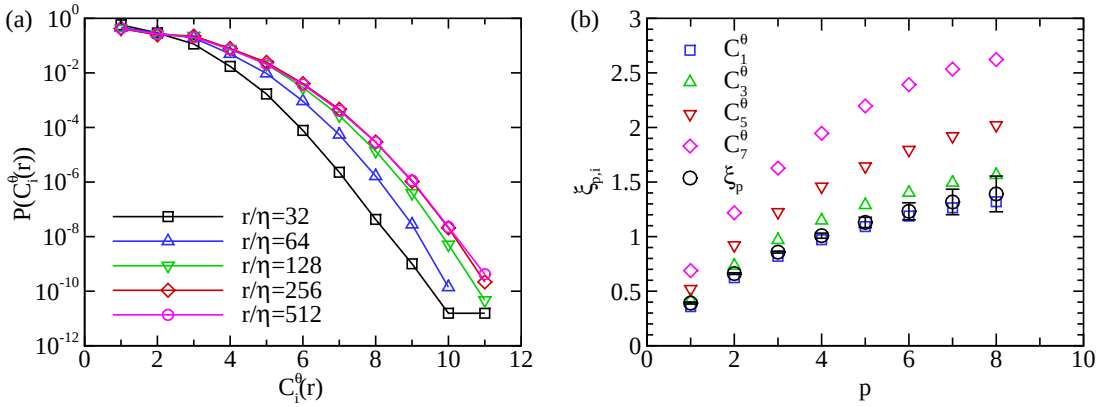

Figure 18: Statistical results of OS subclasses of passive scalar at filter width $\Delta = r/4$. (a) Probability density functions of OS subclasses. (b) Absolute scalings of structure functions in each OS subclass and the overall field.

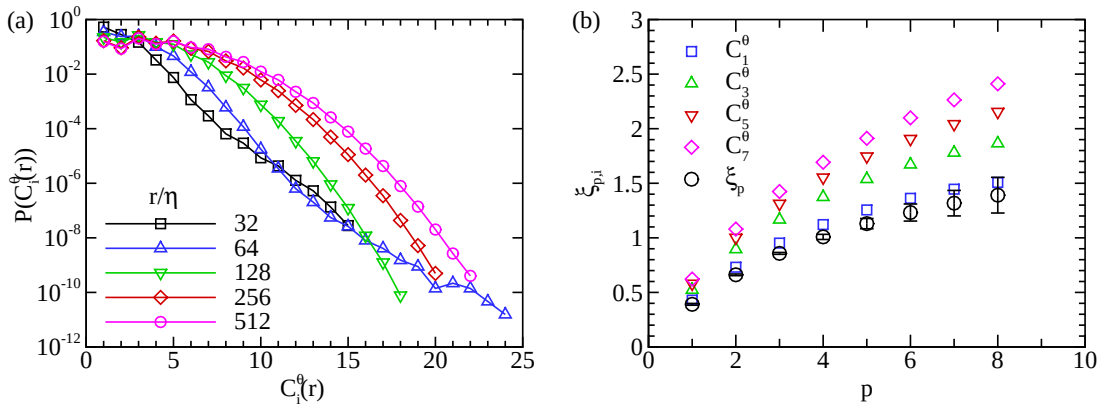

Figure 19: Statistical results of OS subclasses of passive scalar at filter width $\Delta = r/16$. (a) Probability density functions of OS subclasses. (b) Absolute scalings of structure functions in each OS subclass and the overall field.

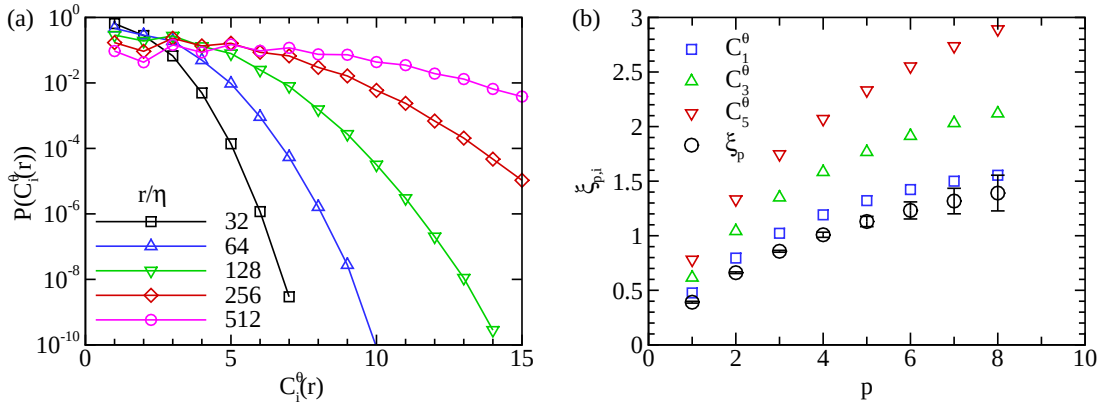

Figure 20: Statistical results of OS subclasses of passive scalar at filter width $\Delta = 16\eta$. (a) Probability density functions of OS subclasses. (b) Absolute scalings of structure functions in each OS subclass and the overall field.

subclass depart from ξ_p significantly, as shown in Fig. 20(b). We have also tested filter width $\Delta = 32\eta$ and the results are similar. Thus when a fixed filter width is used, no scale-invariant property can be observed and the relation $\xi_{p,1} \approx \xi_p$ can not be satisfied either.

In summary, the filter process is important for discerning the inertial-range oscillation structures clearly. A proper, scale-dependent filter width should be chosen to ensure the scale-invariance for PDFs of these structures, which results in the relation that anomalous scaling is determined by the C_1 subclass. However, it does not mean that the collapse of $P(C_i(r))$s is an artificial result, since only the existence of the scale-invariance can lead to the same $P(C_i(r))$ at different r.

References

[1] A. N. Kolmogorov, Dissipation of energy in the locally isotropic turbulence, C. R. Acad. Sci. URSS, 32 (1941), 16.

[2] A. N. Kolmogorov, The local structure of turbulence in incompressible viscous fluid for very large Reynolds numbers, C. R. Acad. Sci. URSS, 30 (1941), 301-305.

[3] U. Frisch, Turbulence: The legacy of A. N. Kolmogorov, Cambridge University Press, 1995.

[4] S. Grossmann, D. Lohse and A. Reeh, Different intermittency for longitudinal and transversal turbulent fluctuations, Phys. Fluids, 9 (1997), 3817-3825.

[5] K. R. Sreenivasan and R. A. Antonia, The phenomenology of small scale turbulence, Annu. Rev. Fluid Mech., 29 (1997), 435-472.

[6] B. Dhruva, Y. Tsuji and K. R. Sreenivasan, Transverse structure functions in high-Reynolds-number turbulence, Phys. Rev. E, 56 (1997), R4928.

[7] T. Gotoh, D. Fukayama and T. Nakano, Velocity field statistics in homogeneous steady turbulence obtained using a high-resolution direct numerical simulation, Phys. Fluids, 14 (2002), 1065-1081.

[8] T. Ishihara, T. Gotoh and Y. Kaneda, Study of high Reynolds number isotropic turbulence by direct numerical simulation, Annu. Rev. Fluid Mech., 41 (2009), 165-180.

[9] R. Benzi, L. Biferale, R. Fisher, D. Q. Lamb and F. Toschi, Inertial range Eulerian and Lagrangian statistics from numerical simulations of isotropic turbulence, J. Fluid Mech., 653 (2010), 221-244.

[10] R. Grauer, H. Homann and J.-F Pinton, Longitudinal and transverse structure functions in high-Reynolds-number turbulence, New J. Phys., 14 (2012), 063016.

[11] Z. Warhaft, Passive scalars in turbulent flows, Annu. Rev. Fluid Mech., 32 (2000), 203-240.

[12] T. Gotoh and P. K. Yeung, Passive scalar transport in turbulence: a computational perspective, in Ten chapters in turbulence, Cambridge University Press, 2012.

[13] A. M. Obukhov, Structures of the temperature field in a turbulent flow, IZv. Akad. Nauk SSSR. Ser. Geogr. Geofiz., 13 (1949), 58-69.

[14] S. Corrsin, On the spectrum of isotropic temperature fluctuations in an isotropic turbulence, J. Appl. Phys., 22 (1951), 469-473.

[15] A. N. Kolmogorov, A refinement of previous hypotheses concerning the local structure of turbulence in a viscous incompressible fluid at high Reynolds number, J. Fluid Mech., 13 (1962), 82-85.

[16] A. M. Oboukhov, Some specific features of atmospheric tubulence, J. Fluid Mech., 13 (1962), 77-81.

[17] C. Meneveau and K. R. Sreenivasan, Simple multifractal cascade model for fully developed turbulence, Phys. Rev. Lett., 59 (1987), 1424-1427.

[18] Z.-S. She and E. Leveque, Universal scaling laws in fully developed turbulences, Phys. Rev. Lett., 72 (1994), 336-339.

[19] S. Chen, K. R. Sreenivasan, M. Nelkin and N. Cao, Refined similarity hypothesis for transverse structure functions in fluid turbulence, Phys. Rev. Lett., 79 (1997), 2253-2256.

[20] C. W. V. Atta, Influence of fluctuations in local dissipation rates on turbulent scalar characteristics in the inertial subrange, Phys. Fluids, 14 (1971), 1803-1804.

[21] Y. Zhu, R. A. Antonia, and I. Hosokawa, Refined similarity hypothesis for turbulent velocity and temperature fields, Phys. Fluids, 7 (1995), 1637-1648.

[22] G. Stolovitzky, P. Kailasnath, and K. R. Sreenivasan, Refined similarity hypotheses for passive scalars mixed by turbulence, J. Fluid Mech., 297 (1995), 275-291.

[23] R. R. Prasad, C. Meneveau, and K. R. Sreenivasan, Multifractal nature of the dissipation field of passive scalars in fully turbulent flows, Phys. Rev. Lett., 61 (1988), 74-77.
[24] N. Cao and S. Chen, An intermittency model for passive-scalar turbulence, Phys. Fluids., 9 (1997), 1203-1205.
[25] R. H. Kraichnan, On Kolmogorov's inertial range theories, J. Fluid Mech., 62 (1974), 305-330.
[26] Z.-S. She, E. Jackson and S. A. Orszag, Intermittent vortex structures in homogeneous isotropic turbulence, Nature, 344 (1990), 226-228.
[27] A. Sain, Manu and R. Pandit, Turbulence and multiscaling in the randomly forced Navier-Stokes equation, Phys. Rev. Lett., 81 (1998), 4377-4380
[28] L. Biferale and I. Procaccia, Anisotropy in turbulent flows and in turbulent transport, Phys. Rep., 414 (2005), 43-164.
[29] R. Camussi, D. Barbagallo, G. Guj and F. Stella, Transverse and longitudinal scaling laws in non-homogeneous low Re turbulence, Phys. Fluids, 8 (1996), 1181-1191.
[30] A. Noullez, G. Wallace, W. Lempert, R. B. Miles and U. Frisch, Transverse velocity increments in turbulent flow using the RELIEF technique, J. Fluid Mech., 339 (1997), 287-307.
[31] W. van de Water and J. A. Herweijer, High-order structure functions of turbulence, J. Fluid Mech., 387 (1999), 3-37.
[32] X. Shen and Z. Warhaft, Longitudinal and transverse structure functions in sheared and unsheared wind-tunnel turbulence, Phys. Fluids, 14 (2002), 370-381.
[33] O. N. Boratav and R. B. Pelz, Structures and structure functions in the inertial range of turbulence, Phys. Fluids, 9 (1997), 1400-1415.
[34] T. Zhou and R. A. Antonia, Reynolds number dependence of the small-scale structure of grid turbulence, J. Fluid Mech., 406 (2000), 81-107.
[35] I. Arad, B. Dhruva, S. Kurien, V. S. Lvov, I. Procaccia and K. R. Sreenivasan, Extraction of anisotropic contributions in turbulent flows, Phys. Rev. Lett., 81 (1998), 5330-5333.
[36] G. P. Romano and R. A. Antonia, Longitudinal and transverse structure functions in a turbulent round jet: effect of initial conditions and Reynolds number, J. Fluid Mech., 436 (2001), 231-248.
[37] T. Zhou, Z. Hao, L. P. Chua and S. C. M. Yu, Scaling of longitudinal and transverse velocity increments in a cylinder wake, Phys. Rev. E, 71 (2005), 066307.
[38] A. Pumir, A numerical study of the mixing of a passive scalar in three dimensions in the presence of a mean gradient, Phys. Fluids, 6 (1994), 2118-2132.
[39] M. Holzer and E. D. Siggia, Turbulent mixing of a passive scalar, Phys. Fluids, 6 (1994), 1820-1837.
[40] K. Yang, Y. Shi, K. R. Sreenivasan and S. Chen, Inertial-range oscillation structures and anomalous scaling of fluid turbulence, (2015), to appear.
[41] M. S. Chong, A. E. Perry and B. J. Cantwell, A general classification of three-dimensional flow fields, Phys. Fluids A, 2 (1990), 765-777.
[42] B. B. Mandelbrot and J. W. V. Ness, Fractional Brownian motions, fractional noises and applications, SIAM Rev., 10 (1968), 422-437.
[43] B. Vreman, B. Geurts, and H. Kuerten, Large-eddy simulation of the turbulent mixing layer using the Clark model, Theor. Comput. Fluid Dyn., 8 (1996), 309-324.
[44] B. Vreman, B. Geurts, and H. Kuerten, Large-eddy simulation of the turbulent mixing layer, J. Fluid. Mech., 339 (1997), 357-390.
[45] P. Abry and F. Sellan, The wavelet-based synthesis for the fractional Brownian motion proposed by F. Sellan and Y. Meyer: remarks and fast implementation, Appl. Comp. Harmonic Anal., 3 (1996), 377-383.

[46] M. A. B. Narayanan, Universal trends observed in the maxima of the longitudinal velocity fluctuations and the zero crossings turbulent flows, AIAA J., 17 (1979), 527-529.
[47] K. R. Sreenivasan, A. Prabhu and R. Narasimha, Zero-crossings in turbulent signals,, J. Fluid Mech., 137 (1983), 251-272.
[48] P. Kailasnath and K. R. Sreenivasan, Zero crossings of velocity fluctuations in turbulent boundary layers, Phys. Fluids A, 5 (1993), 2879-2885.
[49] K. R. Sreenivasan and A. Bershadskii, Clustering properties in turbulent signals, J. Stat Phys., 125 (2006), 1145-1157.
[50] D. Poggi and G. Katul, Flume experiments on intermittency and zero-crossing properties of canopy turbulence, Phys. Fluids, 21 (2009), 65103.
[51] D. Cava, G. G. Katul, A. Molini and C. Elefante, The role of surface characteristics on intermittency and zero-crossing properties of atmospheric turbulence, J. Geophys. Res., 117 (2012), D01104.
[52] R. Benzi, S. Ciliberto, R. Tripiccione, C. Baudet, F. Massaioli and S. Succi, Extended self-similarity in turbulent flows, Phys. Rev. E, 48 (1993), R29.
[53] J. Martin, A. Ooi, M. S. Chong and J. Soria, Dynamics of the velocity gradient tensor invariants in isotropic turbulence, Phys. Fluids, 10 (1998), 2336-2346.
[54] C. Meneveau, Lagrangian dynamics and models of the velocity gradient tensor in turbulent flows, Annu. Rev. Fluid Mech., 43 (2011), 219-245.
[55] R. A. Antonia, A. J. Chambers, D. Britz and L. W. B. Browne, Organized structures in a turbulent plane jet: topology and contribution to momentum and heat transport, J. Fluid Mech., 172 (1986), 211-229.